Physics and Chemistry of Minerals (2026) 53:4
https://doi.org/10.1007/s00269-026-01338-y

Coherent lamellar phase decomposition of alkali feldspar studied by a microscopic approach

Artur Benisek[1] · Edgar Dachs[1] · Gregor Zickler[1] · Rainer Abart[2]

Received: 4 August 2025 / Accepted: 8 January 2026 / Published online: 9 February 2026

Abstract
The Gibbs energy due to coherency strain associated with lamellar phase decomposition, including vibrational components, was investigated, using a microscopic perspective combining atomistic calculations based on density functional theory and calorimetric measurements. The model was applied to the lamellar decomposition of alkali feldspar, revealing that the coherency strain energy coefficient does not only depend on temperature and starting composition, as is the case within the macroscopic, i.e., continuum-mechanical approach, but it also depends on the chemical gradient at the lamellar interfaces and on the lamellar thickness. This difference to the macroscopic approach is caused by a realistic relaxation of the structure in the interior of the lamellae. The coherency strain energy coefficient decreases with decreasing chemical gradient. However, the lowering of the chemical gradient causes the unmixing process to be incomplete increasing the Gibbs energy of mixing, which destabilises lamellae with small chemical gradients. This incompleteness of the unmixing process was quantified in a correction procedure, which was then used to calculate the correct Gibbs energy of mixing. A minimisation procedure of the Gibbs energy that contains components from both mixing and coherency strain resulted in the determination of the equilibrium chemical gradient at lamellar interfaces and its dependence on temperature and lamellar thickness. Although the coherency strain energy coefficient depends on lamellar thickness and chemical gradient, the Gibbs energy minimisation results in a single coherent solvus, which is independent of these properties and is found to agree well with experimental data. The new method can be adapted for coherent lamellar decomposition in other binary solid solutions and alloys.

Keywords Thermodynamics · Precipitation · Exsolution · DFT · Calorimetry · Coherency strain energy · Feldspar

Introduction

Many phases form solid solutions and alloys at high temperatures but tend to unmix and develop precipitates and exsolution microstructures upon cooling. In the early stages of the decomposition process, the interfaces between the newly segregated phases may be coherent. In coherent intergrowths, the crystal structure of the host and the precipitated phases are continuous across the phase boundaries emerging from the unmixing process. In general, the unit cell dimensions of the different homogeneous phases do not match, and thus the phases need to be elastically strained to ensure coherency of the two structures at the interface. The resulting elastic distortion is referred to as *coherency strain*. Cahn and Hilliard (1958) presented a thermodynamic model for a decomposition process producing flat interfaces in isotropic materials, accounting for the elastic strain energy using a continuum-mechanical approach. Their model was expanded to any crystal system by Eshelby (1957), and Lee and Kang (2021). Based on elasticity theory, the coherency strain energy (E) may be written as (Cahn 1962).

$$E = k(X_{\mathrm{B}} - X_{\mathrm{B}}{}^{0})^2 \quad (1)$$

where X_{B} is the mole fraction of the B end-member component in the binary solution, and (X_{B} - $X_{\mathrm{B}}{}^{0}$) is the

Dedicated to Prof. Herbert Kroll on the occasion of his 85th birthday.

✉ Artur Benisek
artur.benisek@plus.ac.at

[1] Chemistry and Physics of Materials, University of Salzburg, Jakob-Haringer-Str. 2a, 5020 Salzburg, Austria

[2] Department of Lithospheric Research, University of Vienna, Josef-Holaubek-Platz 2, 1090 Wien, Austria

compositional deviation of the segregated phase from the starting composition X_B^0. The quantity (X_B - X_B^0) may be regarded as a measure of the degree of decomposition or chemical segregation, and k is the strain energy coefficient. The coherency strain acts against unmixing, and the associated elastic energy adds to the Gibbs energy of mixing, causing the coherent solvus to be lower and narrower than the strain-free solvus. The latter applies when the separated phases have incoherent phase boundaries between them and are free of coherency strain. The strain associated with coherent intergrowth may also affect the entropy, so that Eq. 1) may be written in terms of the Gibbs energy of coherency strain

$$\Delta G^{\mathrm{CS}} = \left(k^h - Tk^s\right)\left(X_{\mathrm{B}} - X_{\mathrm{B}}{}^0\right)^2 \tag{2}$$

where k^h and k^s are the coefficients for the enthalpy and entropy resulting from the coherency strain, ΔH^{CS} and ΔS^{CS}, respectively. In cases where the decomposing solid solution is under pressure (P), a $P\,k^V$ term needs to be added.

In this study, a new microscopic approach is developed to describe the evolution of coherent lamellar intergrowth considering its dependence on temperature, lamellar thickness, and chemical gradient at the lamellar interfaces. To this end, calorimetric measurements and DFT-calculations of ΔG^{CS}, including the excess vibrational entropy caused by the coherency strain, were combined. As a test case, the approach was applied to coherent lamellar intergrowth produced by exsolution of Al/Si disordered alkali feldspar in the binary system $NaAlSi_3O_8$ (Ab) – $KAlSi_3O_8$ (Or). Alkali feldspars possess a framework structure consisting of corner-sharing tetrahedra occupied by Al or Si and irregular cavities occupied by Na or K ions. The distribution of the Al and Si atoms on the tetrahedral sites specifies the symmetry of the structure. At high temperature, the Al/Si distribution is largely disordered consistent with monoclinic symmetry. The respective Ab and Or end members are monalbite and sanidine. At slow cooling, the Al/Si distribution becomes triclinic due to ordering as in low albite (Ab) and microcline (Or). At fast cooling, monalbite transforms displacively into metrically triclinic analbite maintaining its disordered Al/Si distribution. In K-Feldspar, the Al/Si ordering process frequently ends up in a kinetically stranded state called orthoclase characterised by a tweed micro texture. The analbite and orthoclase states both are metastable at any temperature and pressure.

To model coherently decomposed phases, an appropriate formalism for calculating the Gibbs energy of mixing is required, because the compositions of the segregated lamellae generally do not correspond to pure end-member compositions. We applied the mixing model for Al/Si disordered high temperature alkali feldspar of Benisek et al. (2014). It agrees within uncertainties with the calorimetry-based ternary mixing model (Benisek et al. 2010), which is often used in thermodynamic modelling of high temperature rocks because it removes discrepancies between observed and calculated feldspar compositions present in mixing models that are based on phase equilibrium data. Furthermore, to reproduce the low temperature solvus the model can be adjusted by adding a term that reduces the configurational entropy (Benisek et al. 2014).

Coherent lamellar intergrowth of Na-rich and K-rich alkali feldspar was recently studied and modelled based on a phenomenological equilibrium thermodynamic approach combined with elastic theory by Petrishcheva et al. (2023) and Heuser et al. (2024). Furukawa and Tsujimori (2024) used the Cahn-Hilliard model (Cahn and Hilliard 1958) to study coherent lamellar intergrowth from the exsolution of alkali feldspars.

Methods

Thermodynamic models used to describe the thermodynamic mixing behaviour

The Gibbs energy of mixing is written as

$$\Delta G^{\mathrm{mix}} = \Delta H^{\mathrm{mix}} - -T\Delta S^{\mathrm{mix}} \tag{3}$$

where ΔH^{mix} and ΔS^{mix} are the enthalpy and entropy of mixing, respectively. The enthalpy of mixing was modelled using a Margules formulation, i.e.,

$$\Delta H^{\mathrm{mix}} = W^H{}_{\mathrm{AB}}(1 - X_{\mathrm{B}})^2 X_{\mathrm{B}} + W^H{}_{\mathrm{BA}}(1 - X_{\mathrm{B}}) X_{\mathrm{B}}{}^2 \tag{4}$$

where $W^H{}_{\mathrm{AB}}$ and $W^H{}_{\mathrm{BA}}$ are interaction parameters.

The entropy of mixing consists of an ideal and an excess part:

$$\Delta S^{\mathrm{mix}} = S^{\mathrm{mix}}{}_{\mathrm{id}} + S^{\mathrm{mix}}{}_{\mathrm{exc}}. \tag{5}$$

The ideal entropy of mixing is written as

$$S^{\mathrm{mix}}{}_{\mathrm{id}} = -\mathrm{R}\left(X_{\mathrm{B}}\ln(X_{\mathrm{B}}) + (1 - X_{\mathrm{B}})\ln(1 - X_{\mathrm{B}})\right) \tag{6}$$

and describes the configurational entropy of mixing with a random distribution of the two cations mixing on a structural site with site multiplicity of unity, R is the gas constant. For the excess entropy of mixing ($S^{\mathrm{mix}}{}_{\mathrm{exc}}$), an equation analogous to Eq. (4) can be used. It may be separated into a configurational and a vibrational excess part, S^{config} and S^{vib}, respectively.

Table 1 lists the mixing parameters (based on 8 oxygen atoms) and equations used in this study for describing the thermodynamic mixing behaviour of the Al/Si disordered alkali feldspar at solvus temperatures (Benisek et al. 2014).

Adding ΔG^{CS} to ΔG^{mix} yields ΔG^{mix+CS}, the Gibbs energy of mixing including the coherency strain energy. The function ΔG^{mix+CS} (X_K) has two typical minima, as is the case with ΔG^{mix} alone, at conditions corresponding to the two-phase region of the phase diagram. The effects of these quantities on the stability of the solid solution with respect to unmixing may be commented as follows: $S^{mix}{}_{id}$ and $S^{mix}{}_{exc}$ are both positive and due to the negative sign in front of the $T\,\Delta S^{mix}$ term stabilize the solid solution with uniform composition. ΔH^{mix} is positive, which destabilizes the solid solution with uniform composition and is responsible for the decomposition of the homogenous solid solution towards lower temperatures, where the absolute value of the $-T\,\Delta S^{mix}$ term becomes successively smaller and so does its stabilizing effect. The enthalpy due to the coherency strain, ΔH^{CS}, is a positive quantity that only comes into play in coherent intergrowth and makes an aggregate of coherently intergrown exsolved phases energetically less favourable than the corresponding strain free aggregate, und thus acts against exsolution. As a consequence, the coherent solvus lies within the strain-free solvus. When cooling a homogenous alkali feldspar, the unmixing process starts, therefore, at lower temperatures, compared to the case, when strain-free unmixing would occur. ΔS^{CS} has not been investigated so far and is presented here for the first time.

Calculations using density functional theory (DFT)

Quantum–mechanical calculations were based on the DFT plane wave pseudopotential approach implemented in the CASTEP code (Clark et al. 2005; Refson et al. 2006), which is included in the Materials Studio software from Biovia®. The calculations used the local density approximation for the exchange–correlation functional (Ceperley and Alder 1980) and norm-conserving pseudopotentials to describe the core-valence interactions. The $2s^22p^63s^1$, $3s^23p^64s^1$, $3s^23p^1$, $3s^23p^2$, and $2s^22p^4$ electrons were explicitly treated as valence electrons for Na, K, Al, Si, and O, respectively. The DFT parameter settings used in this study are listed in Benisek et al. (2015).

Table 1 Mixing parameters used in this study

	NaK	KNa	Equation	Refs.
W^H (J mol^{-1})	20,083	20,083	Eq. (4)	Hovis (1988)
W^{S_vib} (J mol^{-1} K^{-1})	10.3	10.3	Eq. (4) with H replaced by S^{vib}	Haselton et al. (1983)
W^{S_config} (J mol^{-1} K^{-1})	-7	0	Eq. (4) with H replaced by S^{config}	Benisek et al. (2014)

Structural models for calculating ΔG^{CS}

We studied the following reaction:

$$A + B = A|B, \tag{7}$$

where A|B is the coherently intergrown lamellar structure of A and B. The isolated phases A and B have the same composition and the same Na/K configuration as the A and B lamellae in the coherent A|B intergrowth but were calculated each as separate homogeneous phase paying attention that the structures for A, B and A|B phases are characterised by the same symmetry constraints. The DFT calculated energy difference between the left- and right-hand side of Eq. (7) is the coherency strain energy, $\Delta U_0{}^{CS}$, at a temperature of 0 K, that is present only in A|B. The strain energy due to Na/K mixing in A and B, respectively, is the same in the left- and right-hand side of Eq. (7) and is thus cancelled out. This also applies to the deformation energy stored in monalbite at 0 K that is cancelled out as well. Only three simulations are needed to generate one $\Delta U_0{}^{CS}$ value. Construction of the appropriate supercells for a DFT calculation is straightforward if A and B have end-member compositions and the chemical gradient at the A|B interface is steep. This, however, is not the case if a shallow gradient is assumed across the A|B lamellar boundary and if A and B do not have pure end-member compositions. For these cases, large supercells (up to 624 atoms) need to be constructed to establish a reasonably disordered Na/K-distribution. For simplicity, the crystallographic orientation of the lamellar interface was assumed to be parallel to (100). In natural crystals, the interface is close to (-601) (Laves 1952; Willaime and Brown 1974; Evangelakakis et al. 1993; Heuser et al. 2024). The angular difference between (100) and (-601) amounts to 10°.

Cells with three different Al/Si distributions were investigated in this study: One with a fully disordered distribution obtained by mixing on site (each tetrahedral site was occupied by 0.25 Al and 0.75 Si) generating monoclinic symmetry (P2/m, see Figure A1 in the supplementary material). Another Al/Si distribution has some disorder, but every tetrahedral site is occupied either by Al or Si. Such a structure has triclinic symmetry (P1) and is shown in Fig. A2 (supplementary material). The third Al/Si distribution has a regular Al/Si configuration pattern enabling a monoclinic symmetry (PM, Fig. A3). The three different structures are shown as cif files in the supplementary materials. Further details about the investigated structural models are presented in the supplementary material A.

The DFT-calculated energies ($\Delta U_0{}^{CS}$) must be converted to enthalpies at 298.15 K ($\Delta H_{298.15}{}^{CS}$). $\Delta U_0{}^{CS}$ and $\Delta H_0{}^{CS}$ are related by the volume term $P\,\Delta V_0{}^{CS}$. This term can, however, be neglected, since $\Delta V_0{}^{CS}$ is expected to be small. To

convert ΔH_0^{CS} to room temperature, the heat capacity difference between A+B and the A|B coherent lamellar intergrowth (ΔC_P^{CS}) must be considered, i.e.,

$$\Delta H_{298.15}{}^{CS} = \Delta H_0{}^{CS} + \int \Delta C_P{}^{CS} dT \quad (8)$$

However, as we will see later, only very thin lamellae are characterised by a ΔC_P^{CS} that is not negligible.

Feldspar sample

For determining the heat capacity and vibrational entropy, feldspar samples were prepared as follows. The starting material was a K-rich gem-quality sanidine from Itrongay, Madagascar, with Ab_8Or_{92} composition. The space group is C2/m, the distribution of Al and Si atoms onto the tetrahedral sites is largely disordered ($0.5 < 2t_1 = 0.69$, Heuser et al. 2024; for more details see Kroll and Ribbe 1987). The original composition was shifted to $Ab_{58}Or_{42}$ by cation exchange in a $Na_{0.8}K_{0.2}Cl$ salt melt at 850 °C, 1 bar for 28 days in an evacuated quartz-glass tube heated in a muffle furnace. The exchanged crystals were then heat-treated in an evacuated quartz-glass tube in muffle furnaces for 32 days at 550 °C and 1 bar. After this heat treatment, the samples were quenched in water to room temperature. The heat treatment condition is within the two-phase region of the alkali feldspar phase diagram so that a lamellar, coherently intergrown microstructure could develop. The results of the TEM investigation of the decomposed samples are given in the supplementary material B.

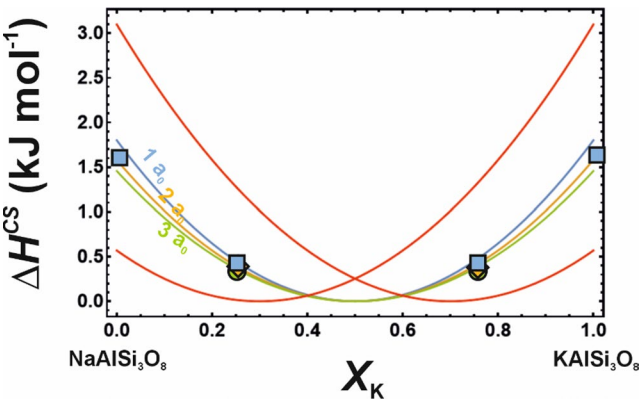

Fig. 1 Coherency strain enthalpy plotted against the mole fraction of K for lamellar thicknesses of 1, 2 and 3 a_0 and a starting composition of $X_K{}^0 = 0.5$. Note, that ΔH^{CS} is symmetrical about $X_K{}^0 = 0.5$, i.e., the values at $X_K = 0$ and 1 (0.25 and 0.75) are based on one DFT value. For the red lines, $X_K{}^0 = 0.3$ and 0.7

STEM investigation

The decomposed sample was milled, and the finest particles of the powder were dispersed on a 400-mesh copper Quantifoil TEM grid, which was coated with a 10 nm thick amorphous carbon film with periodic holes. For characterization of the sample morphology and chemical composition by scanning transmission electron microscopy (STEM), the JEOL JEM-F200 transmission electron microscope at the University of Salzburg was used (operated at 200 kV). The microscope was equipped with a cold field emission electron source and a large, windowless JEOL Centurio EDX (Energy Dispersive X-ray emission) detector (100 mm2, solid angle of 0.97 sr, and energy resolution below 133 eV@ MnKα). STEM bright field images and quantitative EDX data were obtained using a beam current of 0.1 nA and a beam diameter of 0.16 nm.

Calorimetry

The low temperature heat capacity was measured with a relaxation calorimeter (Physical Properties Measurements System (PPMS), Quantum Design®) between 5 and 300 K using the measurement technique described, e.g., by Dachs and Benisek (2011). The sample powder (~10 mg) was put into an Al cup (~8 mg) made from an Al foil. It was pressed into a cylindrical pellet (0.5 mm thickness, 5 mm in diameter), with the Al foil surrounding the sample powder. The pellet was then attached to the sample platform. From each sample, up to three pellets were prepared and measured. The high temperature heat capacity was measured using a Perkin Elmer Diamond DSC® instrument. The method used in this study is given elsewhere (Benisek et al. 2012). The measurements were performed between 273 and 573 K on samples weighing approximately 30 mg. Each sample was prepared in two different pans, each of which was measured three times. The uncertainties of the calorimetric results were studied in Dachs and Benisek (2011) and could also be used here.

Results

Coherency strain energy

In Fig. 1, the coherency strain enthalpy (ΔH^{CS}) is plotted as a function of the mole fraction of K. The plotted functions are based on the DFT calculated values and Eq. (2), without considering the entropy term ($T k^S$), i.e.,

$$\Delta H^{CS} = k^h (X_K - -X_K{}^0)^2 \quad (9)$$

For a lamellar thickness of $d = 1\ a_0$ cell axis length, two different computations were carried out (blue squares in Fig. 1). In the first computation, the lamellae were given end-member compositions; in the second computation, the compositions were chosen as $Ab_{75}Or_{25}$ and $Ab_{25}Or_{75}$. For both compositional variants, ΔH^{CS} can be described reasonably well with one function (blue line in Fig. 1).

Using Eq. (9), the coherency strain enthalpy has the same values for both the Na-rich and the K-rich lamellae, if the starting composition is $X_K{}^0 = 0.5$. Strictly speaking, Eqs. (1, 2 and 9) are only valid if the solvus is symmetric. This is not the case for the alkali feldspar system. Its solvus is slightly asymmetric with a centre at $X_K \cong 0.4$. Nevertheless, Eq. (1) was recently used to successfully describe the coherent solvus (Petrishcheva et al. 2023; Heuser et al. 2024). For $X_K{}^0 = 0.3$ and 0.7 (red lines in Fig. 1), different coherency strain enthalpies are, however, obtained for the Na-rich and the K-rich lamellae.

We did not find a proper way to successfully investigate the asymmetric behaviour due to $X_K{}^0 \neq 0.5$ by DFT calculations. Using Eq. (7), only the whole assemblage can be studied, and this gives one DFT value. We, therefore, assumed that Eq. 9) describes the coherency strain enthalpy of alkali feldspars well, also for cases where $X_K{}^0 \neq 0.5$.

Coherency strain at lamellar interfaces

In our microscopic treatment, the lamellar boundaries are parallel to the *b*, *c*-plane and are considered as more or less gradual compositional transitions extending over a width of up to 2 a_0 unit cell parameters in the crystallographic *a*-direction. For DFT modelling, lamellar boundaries are implemented by changing gradually the ratio of Na and K atoms on the alkali sites, and thus ΔX_K along the crystallographic *a*-direction (see supplementary material A).

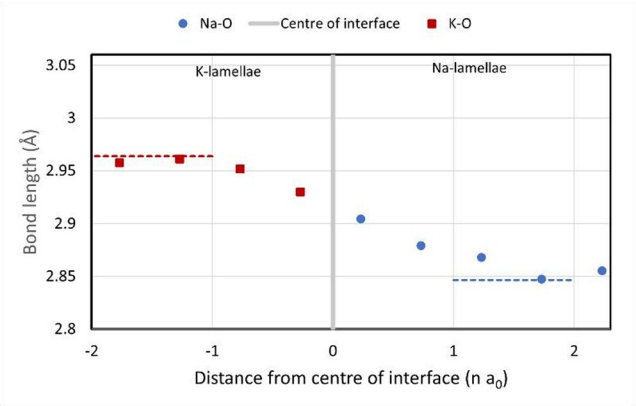

Fig. 2 Variation of the mean Na-O and K-O bond lengths across a (100) oriented lamellar interface in a coherently decomposed phase with $d = 3\ a_0$ and $\nabla = 0.5\ \Delta X_K/a_0$ based on a coordination number of CN = 9. The horizontal dashed lines represent the bond lengths in the centre of the separated lamellae

The compositional gradient in the centre of the transition zone, henceforth referred to as the *compositional gradient at the lamellar boundary*, $\nabla = \Delta X_K/a_0$ and the extension of the transition zone in the *a*-direction is determined by the way the compositional transition is implemented. Our DFT calculations reveal that the resulting coherency strain as inferred from the changes in the Na-O and K-O bonds is localized mainly at the interfaces between the Na- and K-rich lamellae, i.e., at the lamellar boundaries. This is shown in Fig. 2, where the mean DFT calculated bond lengths of the dominantly strained Na-O and K-O polyhedra are plotted against the distance in *a*-direction from the centre of the lamellar interface. The investigated cell has a monoclinic symmetry (Pm), a lamellar thickness of $d = 3\ a_0$ and the compositional transition at the lamellar boundary was set to yield a chemical gradient of $\nabla = 0.5\ \Delta X_K/a_0$. As a result of this compositional gradient, the compositional transition extends to $\pm 1\ a_0$ away from the centre of the lamellar interface into the two lamellae. The lamellar boundary may thus be considered to have a width of $2\ a_0$. It can be seen in Fig. 2 that the mean Na-O bond length increases towards the interface, whereas the mean K-O bond length decreases. At the centres of the Na- and K-rich lamellae, the bond lengths agree with those in the centre of the separated lamellae, as indicated by the horizontal dashed lines.

It can further be seen from Fig. 2 that the increase of the mean Na-O bond length is more pronounced than the decrease of the mean K-O bond length, with the relative bond length changes being 2.0 and −1.0% for Na-O and K-O bonds, respectively. This is similar to the bond length changes along the binary solid solution series in homogenous alkali feldspar when compared to their bond lengths in the end member structures (Benisek et al. 2015). This behaviour causes positive excess heat capacities because the bond softening is more pronounced than the bond stiffening (Benisek and Dachs 2012). In cases where the lamellae are sufficiently thin and the lamellar boundaries represent a significant fraction of the total volume of the lamellar intergrowth, it is, therefore, to be expected that the vibrational entropy of coherently decomposed samples is elevated relative to homogenous samples.

In the case of coherency, relaxation of the cell dimensions is only possible in the direction perpendicular to the lamellar interface (Willaime and Brown 1974). This structural condition is verified by transmission electron microscopic studies showing diffraction spots that are elongated perpendicular to the lamellar interface (Cadoret and Delavignette 1969; Owen and McConnel 1971, Menna et al. 2008) or even split, yielding two diffraction spots aligned in the direction perpendicular to the lamellar interfaces (Heuser et al. 2024).

In the light of these facts, the question arises, how are the bond length changes seen in Fig. 2 possible at all? For the answer, another coherently decomposed cell with high regularity was investigated. This cell has P2/m symmetry, in agreement with an Al/Si distribution of 0.25 Al and 0.75 Si on each tetrahedral site, and a sharp compositional jump at the lamellar interface as well as end member compositions within the lamellae. This cell enabled us to study the bond length changes in more detail. Two types of bonds are considered separately, i.e., the bond that is subparallel to the *a**-direction (normal to the *b*, *c*-plane) and the bonds that are subparallel to the *b*, *c*-plane. The study of this cell shows similar behaviour compared to Fig. 2. The bond length changes, however, extend here into the interior of the lamellae until the bond lengths are as relaxed from coherency strain as possible shown for the monalbite lamellae in Fig. 3.

The bond that is subparallel to the *a**-direction (green lines in Fig. 3) show much stronger variations compared to those that are subparallel to the *b*, *c*-plane (orange lines in Fig. 3). Both bond types (subparallel to the *a**-direction vs. subparallel to the *b*, *c*-plane), however, have components that are parallel to the *a**-direction. The angles between the two bond types and the *a**-direction are ca. 10 and 80°, respectively. A contraction of 0.15 Å in the *a**-direction reduces the lengths of the two bond types by 0.15 and 0.03 Å, respectively, and hence the reduction seen in Fig. 3. The structural unit that is responsible for this contraction is the four-membered tetrahedral ring, where rotations and tilts of the tetrahedra compress these rings in *a**-direction. This observation is in perfect agreement with the situation that relaxation of the cell dimensions is possible but only in the direction perpendicular to the lamellar interface.

Observations on natural alkali feldspars show that the a_0 lattice parameter is shortened in the Na-rich lamellae and elongated in the K-rich lamellae of the strained feldspar compared to the unstrained feldspar (Keefer and Brown 1978; Kroll and Ribbe 1987; their Fig. 8). Note, that the term "unstrained" is here used in the sense that the structure is free of coherency strain, but not free of compositional strain due to mixing.

The DFT calculated cell from Fig. 3 indeed shows that the a_0 lattice parameter in the interior of the monalbite lamellae is shorter than in the unstrained monalbite. This behaviour and the opposite case for the sanidine lamellae can be judged from Table 2.

A large contraction of the monalbite lamellae normal to the *b*, *c*-plane is necessary to obtain relaxation of the Na-O bond lengths causing a strained, short a_0 lattice parameter. This observation may be interpreted as a reduction of energetically unfavourable strain (Na, K-O bond lengths) at the expense of a simultaneous increase of energetically favourable strain (tetrahedral tilt and rotation).

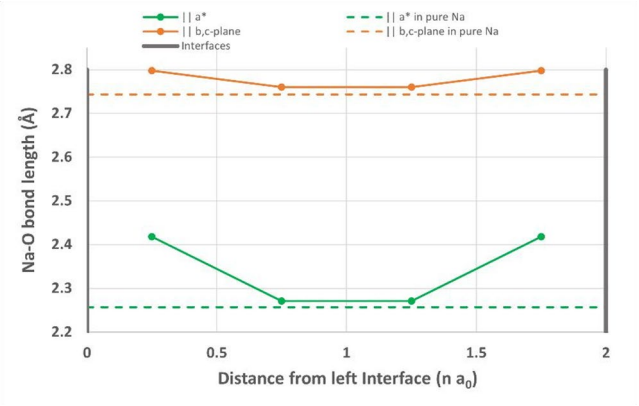

Fig. 3 Variation of the Na-O bond lengths across a (100) oriented monalbite lamella with $d=2$ a_0 in a coherently decomposed phase with sharp interfaces and end member compositions. Two types of bonds are considered with angles to the *a**-direction of 10° and 80° marked by green and orange lines, respectively. The horizontal dashed lines represent the bond lengths in the monalbite

Table 2 Cell edge lengths in units of Å for DFT-investigated feldspars free of strain due to mixing and coherency (unstrained) compared to those strained only by coherency

	a_0	b_0	c_0
Pure monalbite, C2/m, unstrained	8.007	12.881	7.113
Pure sanidine, C2/m, unstrained	8.440	12.999	7.154
Pure monalbite lamellae, P2/m, strained due to coherent intergrowth	7.964	12.947	7.135
Pure sanidine lamellae, P2/m, strained due to coherent intergrowth	8.452	12.947	7.135

Analysing Fig. 3 in still more detail, it can be assumed that the lamellae are too thin to achieve relaxed Na-O bonds. Strain around a point defect propagates at least 10 Å away, which has been shown for many silicates (Figowy et al. 2021). This distance corresponds to ~1.25 a_0 in the monalbite lamellae (Table 2), which is larger than the distance between centre and interface of such lamellae. It must, therefore, be expected that in cases where the lamellae would have a larger width, the Na-O bonds that are subparallel to the *b*, *c*-plane will further relax, so that their lengths approach almost the values of the unstrained monalbite (orange dashed line in Fig. 3). This is because there are more bonds that are subparallel to the *b*, *c*-plane (4 bonds) compared to the one that is subparallel to the *a**-direction. It is, therefore, energetically helpful for the crystal to relax the bonds that are subparallel to the *b*, *c*-plane to a greater extent compared to the other type of bonds. This would need a further contraction of the monalbite lamellae normal to the *b*, *c*-plane. However, in such a case, the other type of bond would attain lengths that may be shorter than in the unstrained monalbite. This is, however, what is observed in experiments as demonstrated for the opposite case (K-O

bonds) in Griffen and Johnson (1984; their Fig. 1). The K-O_{A2} bond is longer than in the unstrained feldspar because this is the bond that is aligned subparallel to the a*-direction, while the other bonds show differences between strained and unstrained feldspar that are smaller or even zero. Note, that also here, the term "unstrained" means that it is free of coherency strain. Investigations on natural feldspar observe both the coherency strain and the compositional strain (Willaime and Brown 1974; their Fig. 1). This is, however, not the case when investigating Eq. (7) by DFT methods. Here, only the coherency strain is observed since the compositions and Na/K configurations of A and B are equal in both the left- and right-hand side of this equation. In the case of such an ideal relaxation it is to be expected that the bond length differences between strained and unstrained crystal are cancelled out, when averaging them. And this is exactly what is observed in Fig. 2, where the mean bond lengths in the centre of the lamellae have the same value compared to the unstrained samples (red and blue dashed lines in Fig. 2).

Note that the findings presented here are fundamentally different from the macroscopic approach (Robin 1974; Willaime and Brown 1974; Petrishcheva et al. 2023), where the lamellar boundaries are treated as sharp interfaces and the compositions are assumed to be uniform throughout the Na-rich and K-rich lamellae with sharp compositional jumps at lamellar interfaces. Applying elastic theory to such a configuration yields elastic strain and stress, which, in general, is different between the two types of lamellae but is homogeneous within each lamellar type, which is an inherent limitation of the macroscopic approach as discussed by Willaime and Brown (1974).

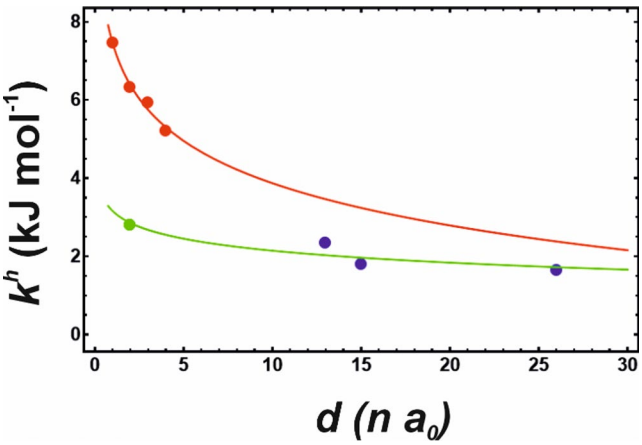

Fig. 4 Coherency strain enthalpy coefficient (k^h) as a function of lamellar thickness (d). The upper curve depicts samples with $\nabla = 1\ \Delta X_K/a_0$, the lower with $\nabla \approx 0.5\ \Delta X_K/a_0$. The blue data points were extracted from Heuser et al. (2024)

ΔH^{CS}-coefficient (k^h) as a function of lamellar thickness (d)

The coherency strain enthalpy coefficient (k^h) is plotted against lamellar thickness in Fig. 4, which shows an exponential decrease of k^h with d.

Changes in the Al/Si distribution that have been performed during the DFT calculations have only a minor effect on k^h. However, k^h also depends on the chemical gradient (∇) at the lamellar interfaces. Since the strain is localized mainly at the lamellar interfaces, such behaviour is to be expected. The upper curve in Fig. 4 corresponds to $\nabla = 1\ \Delta X_K/a_0$, whereas the lower curve corresponds to $\nabla \approx 0.5\ \Delta X_K/a_0$. One value of this curve was DFT calculated and has exactly $\nabla = 0.5$, the others were extracted from the compositional data of samples M-480-64, M-520-32, and M-560-64 from Heuser at al. (2024) by adjusting the k^h values. The ∇´s of their samples result from their atom probe tomography (APT) data, which yield low compositional gradients ($\nabla = 0.1\ \Delta X_K/a_0$) in two cases, but one of their APT experiments yields a steep compositional gradient of $\nabla = 1.2\ \Delta X_K/a_0$. We averaged the ∇´s resulting in $\nabla = 0.47\ \Delta X_K/a_0$. At about 480 °C, the monoclinic/triclinic phase transition in the alkali feldspar (Kroll et al. 1980) crosses the experimentally determined coherent solvus of Heuser et al. (2024). Only data from experiments above 480 °C were, therefore, used for this analysis, because below this temperature, the Na-rich lamellae is triclinic, producing the striking zig-zag interface, which is suspected to increase the degree of semi-coherency of the lamellar interfaces. The lamellar thicknesses of the samples in Heuser et al. (2024) can be well described by $d \sim t^{1/3}$ relation (Busek et al. 1980), which were used to evaluate d of the above samples from other samples where d is known. All coherency strain energy data are summarised in a table of the supplementary material C.

The question may arise whether the lamellar compositions reported in Heuser et al. (2024) correspond to equilibrium compositions and thus lie on the coherent solvus or whether they represent quenched intermediate stages of the chemical segregation process. This was addressed by Heuser et al. (2024) by means of time series experiments, which revealed that after an initial segregation phase the lamellar compositions of the exsolved sanidine from Madagascar remained constant indicating attainment of equilibrium. Once the binodal compositions were reached, the further evolution was dominated by lamellar coarsening and the formation of compositional plateaus, which are a characteristic feature of samples lying on the coherent solvus. Such stationary lamellar compositions were, however not attained for their sanidine from Volkesfeld, which generally shows less sharply bounded lamellae, which likely did not attain equilibrium compositions during the exsolution

experiments. The different characteristics of the two felspars investigated by Heuser et al. (2024) is also reflected by the electron diffraction patterns, which show clear splitting of reflection spots corresponding to lattice planes sub-parallel to the lamellar interfaces indicating coherent intergrowth of lamellae with two distinct lattices and compositions for the sanidine from Madagascar. The electron diffraction patterns of the sanidine from Volkesfeld, however, show streaks running perpendicular to the lamellar interfaces for the reflections corresponding to lattice planes sub-parallel to the lamellar interfaces, indicating more gradual compositional transitions between the two lamellar types and incomplete chemical segregation. Only the data from the sanidine from Madagascar should be considered to represent the coherent solvus (Heuser et al. 2024).

ΔH^{CS}-coefficient (k^h) as a function of the chemical gradient (∇) at the lamellar interface

In Fig. 5, k^h is plotted against the compositional gradient, ∇, across the lamellar interfaces. The upper curve represents samples with a lamellar thickness of 2 a_0, the lower is for $d = 18\ a_0$. Although the data of the upper curve could be fitted by a linear relationship, an exponential relation was used instead. A linear relation would drive the system to very low ∇'s and thus, to a high coherent solvus. An exponential function was preferred. Nevertheless, there is another consideration that may justify the use of an exponential function. The coherency strain value at $\nabla = 0.5\ \Delta X_K/a_0$ with $d = 2\ a_0$ is probably too low (Exp. Nr. 1 in table C1 with the structure shown in Fig. A2, both are presented in the supplementary materials). Due to the lower ∇, the separated lamellae have average compositions of $Ab_{25}Or_{75}$ and $Ab_{75}Or_{25}$. They are characterised by Na-K gradients and in consequence by a non-negligible coherency strain. The guideline that the Na/K configuration of A or B in the left- and right-hand side of Eq. (7) must be the same, was cancelled for this sample. The Na/K configuration of this sample has been changed to lower the gradients. However, it is difficult to construct cells with such compositions without having Na-K gradients somewhere. As a consequence, the calculated ΔH^{CS} of this sample may be offset by an incomplete reaction (Eq. 7).

Heat capacity and entropy difference between coherently intergrown lamellae and corresponding homogeneous feldspar

For determining the heat capacity caused by the coherency strain (ΔC_P^{cs}), Eq. 7) is again relevant. Consequently, the composition of the lamellae must be known to find the heat capacities of homogeneous feldspars with similar compositions as have the lamellae. The feldspar sample used for

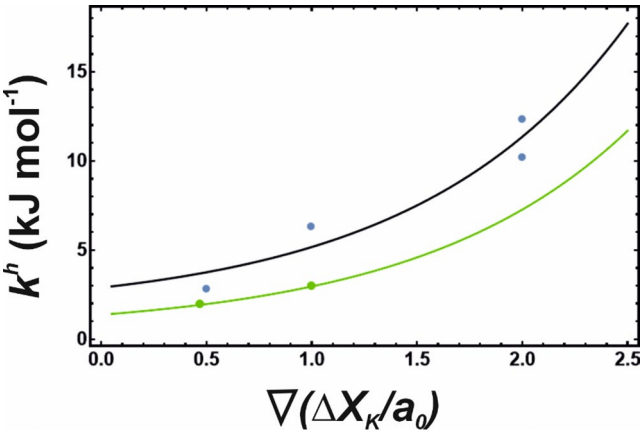

Fig. 5 Coherency strain enthalpy coefficient (k^h) as a function of the chemical gradient, ∇, at the lamellar interfaces. The upper curve depicts samples with $d = 2\ a_0$ (blue points and black line). The samples of the lower curve (green points and line) have $d = 18\ a_0$ and were constructed from the fits in Fig. 3

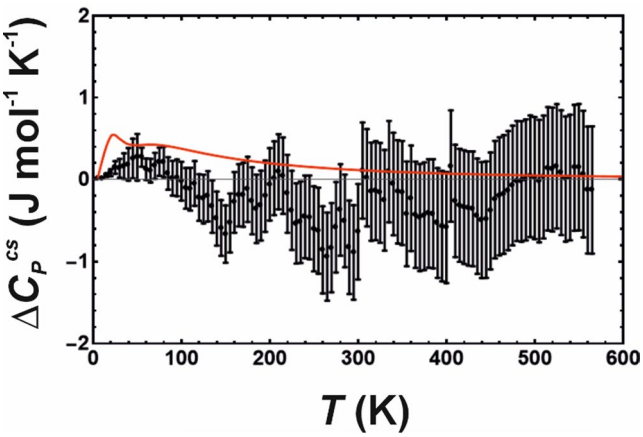

Fig. 6 Excess heat capacity due to coherency strain. Calorimetric data are those with error bars and correspond to samples having a lamellae thickness of ~24 a_0, DFT calculated data ($d = 1\ a_0$) are shown by the red line

calorimetric measurements was therefore investigated by TEM to determine the compositions of the Na- and K-rich lamellae, which were found as ~$Na_{75}K_{25}$ and ~$Na_{40}K_{60}$, respectively. The detailed results are listed in the supplementary material B. The heat capacities of the lamellae free of coherency strain were calculated by interpolating the data of Haselton et al. (1983) for $T < 300$ K and Benisek et al. (2014) for $T > 300$ K. Though the latter authors investigated Al/Si ordered samples, no differences between Al/Si ordered and disordered samples are to be expected at these super ambient temperatures. As shown in Fig. 6, the heat capacity (ΔC_P^{cs}) due to coherency strain inferred from calorimetric measurements is around zero within uncertainties over the entire temperature range. Only at very low temperatures (< 100 K), small positive, and between 100 and

300 K, small negative values are obtained. They result in an entropy due to coherency strain of zero J/mol/K.

For very thin lamellae ($d=1\ a_0$), small positive excess heat capacity values are indicated by DFT calculations (red line in Fig. 6) for temperatures below about 400 K and, hence, a small vibrational entropy of $\Delta S^{CS} = 1.3$ J/mol/K due to coherency strain is inferred. It may be assumed that samples with $d>20\ a_0$ have zero excess vibrational entropies due to coherency strain. At $d<20\ a_0$, the vibrational entropy was treated like ΔH^{CS} due to the lack of data, i.e., they were described by ∇-dependent exponential curves (for more details see the supplementary material D). Nevertheless, the contribution of ΔS^{CS} to ΔG^{CS} is minor, even in samples with thin lamellae.

ΔG^{mix+CS}-difference ($\delta\Delta G^{mix+cs}$) between coherently decomposed and homogenous crystals

For evaluating which ∇, and thus, which k^h value is dominating at a given temperature and a given lamellar thickness, a $\delta\Delta G^{mix+CS}$ function was defined:

$$\delta\Delta G^{mix+CS} = {}^1/_2\,(\Delta G^{mix+CS}{}_{Na} + \Delta G^{mix+CS}{}_{K}) - -\Delta G^{mix}{}_{hom} \qquad (10)$$

where $\Delta G^{mix+CS}{}_{Na}$ and $\Delta G^{mix+CS}{}_{K}$ are the Gibbs energies of mixing including the coherency strain energy of Na- and K-rich lamellae, and $\Delta G^{mix}{}_{hom}$ is the Gibbs energy of mixing of the homogenous sample.

In Fig. 7, this function is plotted against the degree of decomposition, expressed as $X_K - X_K{}^0$, for different compositional gradients at the lamellar interfaces, ∇′s. The curves corresponding to different ∇′s show minima at different $X_K - X_K{}^0$ values.

According to Fig. 7, the lowest $\delta\Delta G^{mix+CS}$ minimum at 460 °C and $d=5\ a_0$ is the one with $\nabla \cong 0.4\ \Delta X_K/a_0$ and at a degree of decomposition of $X_K - X_K{}^0 \cong 0.3$. $X_K{}^0$ was chosen to be in the centre of the strain-free solvus, i.e., $X_K{}^0 = 0.4$, and equal shifts in Na-rich and K-rich directions were assumed. The equilibrated coexisting phases have then compositions of ca. $Na_{90}K_{10}$ and $Na_{30}K_{70}$ and are characterized by a chemical gradient of $\nabla \cong 0.4\ \Delta X_K/a_0$ at their interface.

Since the strain energy decreases with decreasing ∇ (Fig. 5), one would expect that the lowest $\delta\Delta G^{mix+CS}$ minimum is the one with the lowest ∇. However, this is not the case. This is due to the fact that low ∇ values cause a more incomplete decomposition as compared to the decomposition in the case of steeper compositional gradients at the lamellar interfaces. Hence, the curves with $\nabla < 0.4\ \Delta X_K/a_0$ show higher $\delta\Delta G^{mix+CS}$ minima. For low values of ∇, incomplete decomposition suppresses the unmixing process.

ΔH^{mix} and ΔS^{mix} of Eq. (3) must, therefore, be calculated for a corrected composition. The relevant compositions correspond to the mean Na- and K-concentrations in the respective lamellae, but not to their maximal concentrations. The effective degree of decomposition is, thus, reduced when lowering ∇. This has been accounted for when calculating the curves in Fig. 7 and is responsible for the result that the lowest gradient does not produce the lowest $\delta\Delta G^{mix+CS}$ minimum.

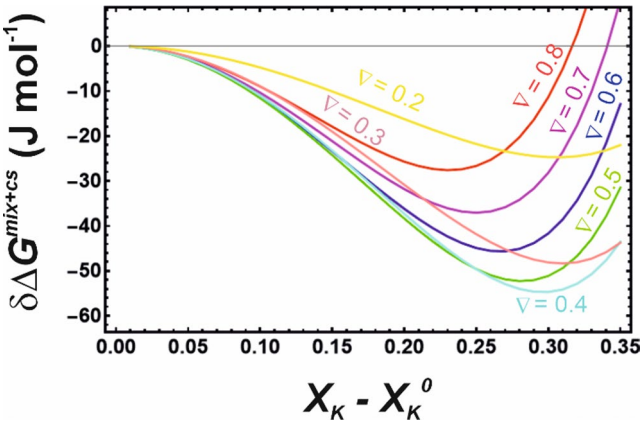

Fig. 7 $\delta\Delta G^{mix+CS}$ function for different chemical gradients (∇, in $\Delta X_K/a_0$) calculated at 460 °C for a lamellar thickness of $d=5\ a_0$

Table 3 Equilibrium gradient values for some temperatures and lamellar thicknesses

	∇ ($\Delta X_K/a_0$)			
	d=2 a_0	d=5 a_0	d=18 a_0	d=30 a_0
T=480 °C	0.56	0.38	0.24	0.25
T=520 °C	0.44	0.32	0.20	0.22
T=560 °C	0.30	0.19	0.15	0.14

However, $X_K - X_K{}^0$ has an influence on the correction. To calculate the $\delta\Delta G^{mix+CS}$ minimum accurately, an iterative procedure was applied to obtain agreement between the $X_K - X_K{}^0$ value used to calculate the corrected decomposition and the $X_K - X_K{}^0$ value of the $\delta\Delta G^{mix+CS}$ minimum (for more details on the calculation of the corrected degree of decomposition, see supplementary material E). This correction is most important when the compositional gradient at the lamellar interfaces becomes small. This is the case at higher temperatures, where the coherent solvus starts to close.

Finding the equilibrium compositions

For each lamellar thickness and temperature, there are a series of $\delta\Delta G^{mix+CS}$ curves based on different ∇′s (Fig. 7). To find the stable one, the $\delta\Delta G^{mix+CS}$ minima were plotted against ∇. A polynomial was fitted to these data, and the minimum of the minima, which corresponds to that ∇ which produces the lowest $\delta\Delta G^{mix+CS}$ minimum, was searched. This ∇ should be the stable one. Some equilibrium gradient values for given temperatures and lamellar thicknesses are listed in Table 3.

Below $d=2\ a_0$, no $\delta\Delta G^{mix+CS}$ minimum was found. The $\delta\Delta G^{mix+CS}$ minimum with the stable ∇ gives the compositions of the two coexisting phases at a given temperature and lamellar thickness under the assumption that the degree of decomposition is equal in both chemical directions when $X_K{}^0 = 0.4$. Applying this procedure at different temperatures, the coherent solvus was estimated (Fig. 8).

The very striking feature here is that the solvus does not depend on lamellar thickness. There exists a single coherent solvus for a given composition of the homogeneous precursor feldspar in good agreement with the experimental data of Heuser et al. (2024), who studied coherently decomposed alkali feldspars with similar starting composition by atom probe tomography.

Discussion

We present a new microscopic approach for quantifying the coherency strain energy associated with compositional gradients across the lamellar boundaries in coherent lamellar intergrowths and discuss its application to the coherent exsolution of alkali feldspar. To this end, we use DFT calculations to determine the microscopic strain, i.e. change in K-O and Na-O bond lengths, in microscopic configurations mimicking macroscopic compositional gradients across the lamellar interfaces relative to the homogeneous crystal structure of the alkali feldspars. Different microscopic configurations were employed to produce a range of compositional gradients across the lamellar interfaces, and different lamellar widths were considered. The associated coherency strain energy was calculated based on the notion that coherency strain causes elastic stresses and that, for sufficiently small strain, i.e., within the limits of linear elasticity, the elastic energy is a quadratic form of the strain as expressed in Eq. 1). The contributions of all relevant elastic constants (interatomic potentials) are combined in the strain-energy coefficient k. Our analysis reveals that the coherency strain due to Na-O and K-O bond length changes is mainly localized at the lamellar interfaces, where compositional gradients prevail. However, a full relaxation in the interior of the lamellae is not possible since the lattice parameters in both directions of the boundary plane must be the same for both lamellar types in the case of coherency. In contrast to a widespread assumption (e.g., Yund and Tullis 1983), the coherently decomposed crystal is not found to be characterised by a homogeneous coherency strain. According to our DFT calculations the crystal shows relaxation of the Na-O and K-O bonds by variations along the direction normal to the boundary plane. These DFT-observations agree with very large r.m.s. amplitudes of atomic vibrations, which were found in refinements of the intergrown structures

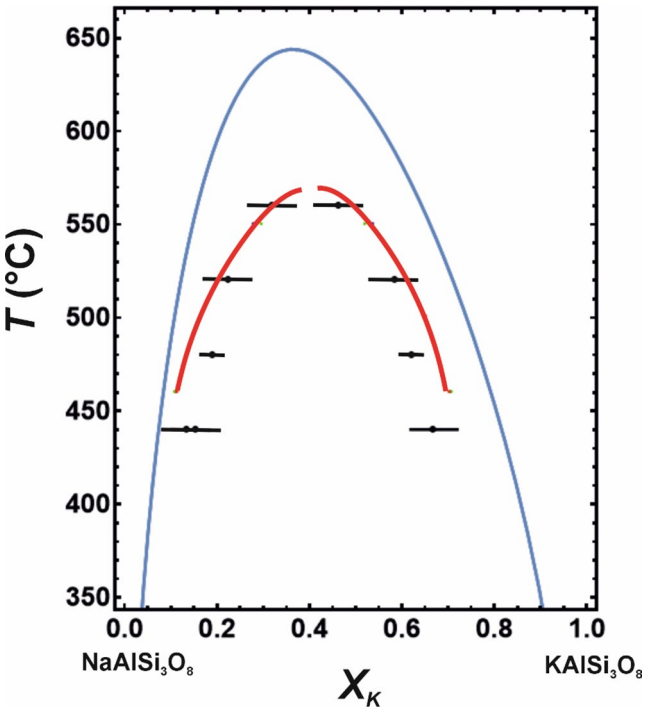

Fig. 8 Different solvi for the alkali feldspar system. Blue solid line: strain free solvus, calculated with data from Table 1. Red solid line: coherent solvus from this study for $d>5\ a_0$. Data points with error bars: experimental data of the coherent solvus from Heuser et al. (2024)

(Keefer and Brown 1978). The authors interpreted the large amplitudes as a "space-averaged disorder caused by a variation in strain".

For lamellar thicknesses of $d>20\ a_0$, the strain energy coefficient in Eq. (1) is essentially independent of temperature and varies with lamellar thickness and the chemical gradient at the lamellar interfaces. Only for very thin lamellae with $d<20\ a_0$, a weak temperature dependence of k, and thus of the Gibbs energy accounting for coherency strain energy may be expected. The temperature dependence of any Gibbs energy contribution is given by the corresponding entropy contribution, as defined in Eq. (2) for the coherency strain energy. The entropy change due to coherency strain is given by the integral of $\Delta C_P{}^{CS}/T\ \mathrm{d}T$. A vibration of a designated chemical bond has its specific frequency and, as a consequence, it is excited at a characteristic temperature. The coherency strain affects the Na-O and K-O bond lengths (Figs. 2 and 3). The vibrations of these bonds are excited at a low temperature of around 60 K (Benisek et al. 2015). If present, our calorimetric experiments (Fig. 6) would have detected such an entropy contribution. For very thin lamellae, the coherency strain has an effect on the heat capacity below 400 K with maxima at 30 and 80 K, producing a positive excess vibrational entropy due to coherency strain. Consequently, k of Eq. (1) decreases with increasing temperature for very thin lamellae. This temperature

dependence of k is, however, not found for lamellae with $d = 24\ a_0$. Here, the coherency strain has almost no effect on the heat capacity and vibrational entropy. At this point, the question arises: What could be the effect of the configurational entropy? Even this part of the entropy can be detected by calorimetric experiments, as demonstrated for Cu_3Au crystals (Benisek and Dachs 2015) if the atomic configuration changes during the calorimetric experiment. This is, however, not to be expected in the case of feldspars, because of the relatively slow Na-K diffusion kinetics compared to that of Cu-Au in the Cu_3Au phase.

The configurational entropy in the alkali feldspar system is changed during the exsolution process, which is accounted for in Eq. (6). The coherency strain reaction (Eq. 7) is thought to have no effect on the Na/K configuration. Otherwise, a significant effect on the vibrational entropy would be expected at ~ 60 K, which is, however, not observed. Hence, no entropy contribution needs to be considered, and therefore, the strain energy coefficient does not depend on temperature for the alkali feldspars in samples with $d > 20\ a_0$.

The method for calculating the coherent solvus introduced in this study has been applied for the starting composition $X_K^0 = 0.4$. This has been done, because the compositional shifts are equal in both directions, i.e. towards more Na-rich and towards more K-rich compositions, for that case. The method may be applied also for other starting compositions. Then, the compositional shifts associated with decomposition are different in both directions and the calculation procedure must be adopted. However, our method is not able to find its own centre of the coherent solvus. It must be assumed that the coherent solvus has the same centre as the strain-free solvus. Starting compositions that deviate significantly from 0.5, cause an asymmetric ΔH^{CS} function (see Fig. 1), which in turn shifts the coherent solvus a little bit to the right or to the left. Therefore, the method introduced in this study is applicable only for starting compositions that do not deviate too much from 0.5. The tangent construction method (touching a common tangent to the two minima of the G-curve) would find the coherent solvus independent of the strain-free solvus. However, until now, no way has been found to implement the important gradient-related correction of the degree of decomposition into this tangent construction method.

Supplementary Information The online version contains supplementary material available at https://doi.org/10.1007/s00269-026-01338-y.

Acknowledgements We thank E. Forsthofer for maintaining the Materials Studio software at the Salzburg University. We are also gratefully for the constructive reviews of B. Dubacq, Paris.

Author contributions Idea and conceptualization: Artur Benisek; Methodology: Artur Benisek; Calculations: Artur Benisek; Formal analysis, sample preparation and investigation: Artur Benisek, Edgar Dachs, Gregor Zickler, Rainer Abart; Writing - original draft preparation: Artur Benisek; Writing - review and editing: Artur Benisek, Edgar Dachs, Gregor Zickler, Rainer Abart; Funding acquisition: Edgar Dachs (P33904), Gregor Zickler (37120633).

Funding Open access funding provided by Paris Lodron University of Salzburg. This research was funded in whole or in part by the Austrian Science Fund (FWF) [https://doi.org/10.55776/P33904]. For open access purposes, the author has applied a CC BY public copyright license to any author accepted manuscript version arising from this submission. TEM measurements were carried out on a JEOL JEM F200 TEM equipped with an energy filter funded by the FFG (grant number 37120633).

Data availability Available data and cif files which are not presented in the text and supplementary materials can be obtained from the first author on request.

Declarations

Conflict of interest The authors have no relevant financial or non-financial interests to disclose.

References

Benisek A, Dachs E (2012) A relationship to estimate the excess entropy of mixing: application in silicate solid solutions and binary alloys. J Alloys Compd 527:127–131

Benisek A, Dachs E (2015) The vibrational and configurational entropy of disordering in Cu_3Au. J Alloys Compd 632:585–590

Benisek A, Dachs E, Kroll H (2010) A ternary feldspar-mixing model based on calorimetric data: development and application. Contrib Mineral Petrol 160:327–337

Benisek A, Kroll H, Dachs E (2012) The heat capacity of fayalite at high temperatures. Am Mineral 97:657–660

Benisek A, Dachs E, Kroll H (2014) Thermochemistry of the alkali feldspars: calorimetric study of the entropy relations in the low albite-low microcline series. Am Mineral 99:76–83

Benisek A, Dachs E, Grodzicki M (2015) First-principles investigation of the lattice vibrations in the alkali feldspar solid solution. Phys Chem Minerals 42:243–249

Busek PR, Gordeon LN, Veblen DR (1980) Subsolidus phenomena in pyroxenes. Rev Mineralogy 7:117–204Jr

Cadoret R, Delavignette P (1969) Ětude de La décomposition spinoïdale Au microscope électronique Dans les alliages cunife. Phys Stat Sol 32:853–865

Cahn J (1962) On spinodal decomposition in cubic crystals. Acta Metall 10:179–183
Cahn JW, Hilliard JE (1958) Free energy of a nonuniform System. I. Interfacial free energy. J Chem Phys 28:258–26733
Ceperley DM, Alder BJ (1980) Ground state of the electron gas by a stochastic method. Phys Rev Lett 45:566–569
Clark SJ, Segall MD, Pickard CJ, Hasnip PJ, Probert MIJ, Refson K, Payne MC (2005) First principles methods using CASTEP. Z Kristallogr 220:567–570
Dachs E, Benisek A (2011) A sample-saving method for heat capacity measurements on powders using relaxation calorimetry. Cryogenics 51:460–464
Eshelby JD (1957) The determination of the elastic field of an ellipsoidal inclusion, and related problems. Proc Royal Soc.
Evangelakakis C, Kroll H, Voll G, Wenk H-R, Meisheng H, Köpcke J (1993) Low-temperature coherent exsolution in alkali feldspars from high-grade metamorphic rocks of Sri Lanka. Contrib Mineral Petrol 114:519–523
Figowy S, Dubacq B, D'Arco P (2021) Crystal chemistry and partitioning of halogens in hydrous silicates. Contrib Mineral Petrol 176:100
Furukawa T, Tsujimori T (2024) The Cahn-Hilliard model of coherent lamellar microstructure: application to alkali feldspar. Contrib Mineral Petrol 179:91
Griffen DT, Johnson BT (1984) Strain in triclinic alkali feldspars: a crystal structure study. Am Mineral 69:1072–1077
Haselton HT, Hovis GL, Hemingway BS, Robie RA (1983) Calorimetric investigation of the excess entropy of mixing in analbite-sanidine solid solutions: lack of evidence for Na,K short-range order and implications for two-feldspar thermometry. Am Mineral 68:398–413
Heuser D, Dubosq R, Petrishcheva E, Bian G, Rentenberger C, Lengauer CL, Gault B, Habler G, Abart R (2024) Coherent solvus of disordered alkali feldspar: experiment, atom probe tomography and thermodynamic model. Contrib Mineral Petrol 179:68
Hovis GL (1988) Enthalpies and volumes related to K-Na mixing and Al-Si order/disorder in alkali feldspars. J Petrol 29:731–763
Keefer KD, Brown GE (1978) Crystal structures and compositions of sanidine and high albite in cryptoperthitic intergrowth. Am Mineral 63:1264–1273
Kroll H, Ribbe PH (1987) Determining (Al,Si) distribution and strain in alkali feldspar using lattice parameters and diffraction-peak positions; a review. Am Mineral 72:491–506
Kroll H, Bambauer HU, Schirmer (1980) The high albite-monalbite and analbite-monalbite transitions. Am Mineral 65:1192–1211
Laves F (1952) Phase relations of the alkali feldspars. II. The stale and Pseudo stable phase relations in the alkali feldspar system. J Geol 60:549–574
Lee HY, Kang SJL (1994) A general equation of coherency strain energy and its application. Z Metallkunde 85:426–443
Menna M, Tribaudino M, Renzulli A (2008) Al-Si order and spinodal decomposition texture of a sanidine from igneous clasts of stromboli (southern Italy): insights into the timing between the emplacement of a shallow basic sheet intrusion and the eruption of related ejecta. Eur J Mineral 20:183–190
Owen DC, McConnell JDC (1971) Spinodal behaviour in an alkali feldspar. Nat Phys Sci 230:118–119
Petrishcheva E, Heuser D, Abart R (2023) Coherent lamellar intergrowth in alkali feldspar. Contrib Mineral Petrol 178:77
Refson K, Tulip PR, Clark SJ (2006) Variational density functional perturbation theory for dielectrics and lattice dynamics. Phys Rev B 73:155114
Robin P (1974) Stress and strain in cryptoperthite lamellae and coherent solvus of alkali feldspars. Am Min 59(11–1):1299–1318
Willaime C, Brown W (1974) A coherent elastic model for the determination of the orientation of exsolution boundaries: application to the feldspars. Acta Crystallogr A 30:316–331
Yund RA, Tullis J (1983) Subsolidus phase relations in the alkali feldspars with emphasis on coherent phases. Rev Mineralogy 2:141–170